Structural order in near-frictionless hydrogenated diamondlike carbon films probed at three length scales via transmission electron microscopy

A. C. Y. Liu,* R. Arenal, and D. J. Miller
Materials Science Division, Argonne National Laboratory, Illinois 60439-4845, USA

Xidong Chen
Cedarville University, Cedarville, Ohio 45314, USA and Electron Microscopy Center, Argonne National Laboratory, Illinois 60439-4845, USA

J. A. Johnson
Nuclear Engineering Division, Argonne National Laboratory, Illinois 60439-4845, USA

O. L. Eryilmaz and A. Erdemir
Energy Systems Division, Argonne National Laboratory, Illinois 60439-4845, USA

John B. Woodford
Nuclear Operations Division, Argonne National Laboratory, Illinois 60439-4845, USA
(Received 15 December 2006; published 1 May 2007)

A series of hydrogenated diamondlike carbon films grown using plasma-enhanced chemical-vapor deposition is systematically studied as a function of source gas composition using transmission electron microscopy. The structure of the films is examined at three distinct length scales. Both plan-view and cross-sectional studies are undertaken to reveal any large-scale inhomogeneities or anisotropy in the films. The degree of medium-range order in the films is measured by performing fluctuation electron microscopy on the plan-view and cross-sectional specimens. Electron-energy-loss spectroscopy is employed to measure the mass density and sp^2:sp^3 carbon bonding ratios of the samples. Thus, inhomogeneity as a function of depth in the film is revealed by the measurements of the short- and medium-range orders in the two different sample geometries. Soft, low-density diamondlike carbon films with low coefficients of friction are found to be more homogeneous as a function of depth in the film and possess reduced medium-range order in the surface layer. We find that these properties are promoted by employing a high hydrogen content methane and hydrogen admixture as the growth ambient. In contrast, harder, denser films with higher coefficients of friction possess a distinct surface layer with a relatively elevated level of carbon sp^3 bonding and a higher degree of medium-range order. The structure of the films is examined in the light of the energetics of the growth process. It appears that a high flux of penetrating hydrogen ions modifies the surface layer containing the remnant damage from the carbon ions, homogenizing it and contributing to a lowering of the coefficient of friction.

DOI: 10.1103/PhysRevB.75.205402 PACS number(s): 61.43.Er, 68.37.Lp

I. INTRODUCTION

Hydrogenated diamondlike carbon (DLC) films are often characterized by single measurements of the sp^2:sp^3 carbon bonding ratio[1] and hydrogen content[2] using large volume probes. While these quantities have been used to explain the felicitous mechanical and optical properties of such films, they do not take into account any possible inhomogeneity or anisotropy. Indeed, both inhomogeneity and anisotropy are detected in two distinct length regimes in DLC films. At the level of microstructure, such deposited films have often been found with distinct layers of different density, reflective of the energetics of the deposition process itself.[3–6] In the same length regime, graphitic structural units have been found to align their c axes with the plane of the film to relieve compressive stress.[4,6–8] At the scale of 1–3 nm, in the realm of medium-range order,[9] recent fluctuation electron microscopy (FEM) measurements suggest that both hydrogen-free and hydrogenated DLC films contain "clusters" with either a graphitic or diamondlike character.[10,11] FEM is sensitive to the three-body and four-body correlation functions in the material,[12,13] and hence, such clusters may be interpreted as "regions of correlated structure"[14] as distinct from micro- or even nanocrystallites. The presence of such clusters cannot be detected unambiguously by standard high-resolution transmission electron microscopy techniques.[15] Raman spectroscopy on DLC films has also suggested that clustering of the sp^2 bonded carbon atoms may be used to distinguish between different DLCs.[16] However, it should be noted that the clusters observed in FEM are not simply related to the graphitic structural units or clusters that give rise to the changes in magnitude and shifts of the D and G peaks in the Raman spectrum of DLC films.[4,16–18] Intensive computer modeling of both the FEM and Raman results using large atomic models accompanied by exacting experiments would be required to make such an identification.

The presence of clusters in DLC films as detected by the FEM studies gives rise to an interesting possibility. Two films may possess the same ratio of sp^2:sp^3 carbon bonding but have completely different medium-range orders due to

TABLE I. Summary of NFC growth parameters and properties (Refs. 11, 19, and 20).

Sample	Source gas composition	Coefficient of friction	Hardness (GPa)	Hydrogen content (at. %)
NFC6	25%CH_4:75%H_2	0.0010	14.0	39±3.9
NFC2	50%CH_4:50%H_2	0.0040	15.7	39±3.9
NFC7	100%CH_4	0.0140	20.8	45±4.5
NFC10	100%C_2H_2	0.27	30.1	

different populations of graphitic and diamondlike (mostly sp^2 and sp^3 bonded, respectively) clusters. In addition, the graphitic and diamondlike clusters may have different sizes and "crystallinities," that is, how closely the local structure approaches a crystalline one. Variations in inhomogeneity at this medium-range of 1–3 nm may influence the mechanical and tribological properties of the film such as the hardness and coefficient of friction.

Here, we investigate the structures of a set of DLC films made by plasma enhanced chemical-vapor deposition (PECVD) using transmission electron microscopy (TEM) techniques. Specifically, we measure the ratio of sp^2:sp^3 carbon bonding and the mass density using electron-energy-loss spectroscopy (EELS) and the degree of medium-range order using FEM. The sp^2:sp^3 carbon bonding ratio is indicative of the short-range ordering of the sample, while medium-range order at the level of 1–3 nm is uncovered using FEM. Larger-scale inhomogeneities and anisotropy are probed through the preparation of both plan-view and cross-sectional TEM samples. We examine different volumes of the films in two mutually perpendicular orientations. Thus, we determine film structure at three very different length scales. This approach has been designed to investigate departures from an entirely homogeneous film that occur specifically in DLC films grown using PECVD. In-plane stresses in these films give rise to one axis for anisotropy which is the plane of the film.[4] The energetics of the growth process seems to indicate that one common type of large-scale inhomogeneity is manifested, a difference between the surface layer and the bulk of the film.[4]

The hydrogenated DLC films that were studied demonstrate strikingly low friction properties and have been dubbed near-frictionless carbon (NFC).[11] The tribology, hydrogen content, and absolute carbon bonding ratios of the NFCs have been reported previously.[11,19,20] The films were made using PECVD with a methane and hydrogen or acetylene atmosphere. The source gas compositions for the different films in the set and their measured properties are summarized in Table I. The coefficient of friction was measured in a dry inert gas atmosphere, and it was discovered that a higher proportion of hydrogen in the source gas imparts superior friction properties onto the resulting film. Specifically, NFC6 possesses the lowest coefficient of friction, with an exceptionally low value of 0.001.[11,20] The mechanical hardness of the films demonstrates a similar trend with greater absolute proportions of hydrogen in the source gas, resulting in a lowered hardness.[21] The hydrogen contents of NFC2, NFC6, and NFC7 were measured using hydrogen forward scattering (HFS) and were found to be the same within their errors.[11,20] The proportion of hydrogen was significant at 40 at. %. Raman spectroscopy was also performed on the films grown using methane environments, and it was found that the parameters extracted from the UV Raman spectra did not vary with source gas composition.[11] The similarity of the Raman spectra and the small variation in hydrogen content of these films would seem to indicate that their structures are almost identical. Such a conclusion is at odds with the widely variant mechanical and tribological properties that the films exhibit. The intensive TEM study reported in this work scrutinizes the structures of the films at three levels and makes significant progress toward resolving these apparent inconsistencies. Moreover, the role of the ion species in the plasma in determining the long- and medium-range homogeneities of the film and the subsequent mechanical and tribological properties is strongly articulated by this work.

This paper is organized in the following manner. In Sec. II, we review the techniques of EELS and FEM. EELS and FEM in the TEM have very different spatial resolutions, and we discuss how we resolve this disparity to allow a meaningful comparison of the structural information gained via each technique. Our low-density films also pose particular problems for their study with FEM. In this same section, we describe and address these issues in relation to thickness effects in the magnitude of the FEM data. The volume of the film that is sampled by each technique is explicitly calculated to allow insight into the DLC growth processes. In Sec. III, we present the measurements of mass density, carbon bonding ratio, and degree of medium-range order. The insights afforded by these measurements into the energetics of the deposition process and the mechanical and tribological properties of the films are detailed in Sec. IV.

II. EXPERIMENT

A. TEM sample geometry

Atomic bonding information can be obtained at high spatial resolution using EELS and scanning transmission electron microscopy (STEM) with a small probe size. This high spatial resolution has been used to study sp^2 bonded 0.4–1.3 nm thick surface layers in highly tetrahedral DLC films.[3,6] In amorphous materials, the EELS signal is generated within the cone defined by the electron beam as it broadens through the thickness of the TEM sample. This broadening is the final limitation on spatial resolution. FEM is a statistical technique that probes fluctuations in the structure of amorphous materials, and so large areas must be sampled by necessity. In this work, the FEM consists of using tilted dark-field imaging[22,23] to probe structural fluctuations. Other FEM techniques employ hollow cone dark field[12] or nanodiffraction in STEM.[24] These last two techniques are conjugate to one another and amount to a rotational averaging of the tilted dark-field technique.[9] In this experiment, each dark-field image corresponds to 240 $\times$ 240 nm^2 in area, and so nanometer resolution is far from obtainable. With this in mind, the changes in medium-range order as a function of depth in the film were examined by preparing both cross-sectional and plan-view samples of the

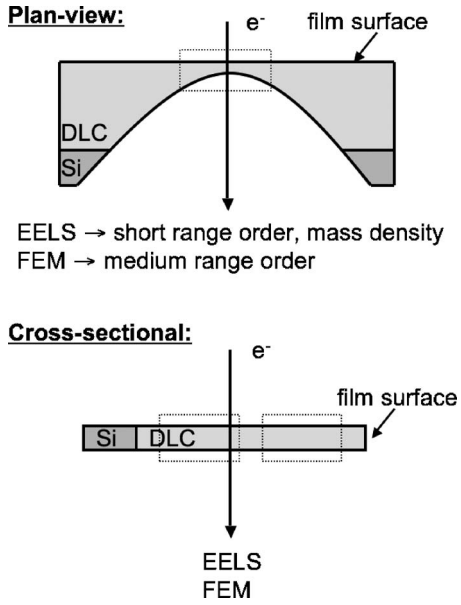

FIG. 1. Plan-view (top) and cross-sectional (bottom) sample geometries. FEM and EELS measurements probe the medium- and short-range orders, respectively, while preparation of the complementary specimen geometries allows different volumes and orientations to be studied by each technique. In the plan-view case, the topmost layer is sampled parallel to the direction of growth. For the cross-sectional samples, the film thickness allowed two FEM measurements to be made perpendicular to the growth direction. The measurement volumes in each case are indicated with a dotted bounding box.

films. The film thickness of ~1 μm permitted two nonoverlapping FEM measurements to be made in the cross-sectional specimens so that any large-scale differences in medium-range order in the bulk could be observed. The FEM measurement of the plan-view specimens sampled the topmost layers and could discern the presence of a surface layer with different medium-range ordering. Additionally, our examination of film structure using FEM in two perpendicular orientations will be sensitive to the slightest anisotropy in the material. The mass density and carbon $sp^2:sp^3$ bonding ratios were measured using EELS on the same set of samples. As these measurements were designed to complement the FEM measurements, modest spatial resolution was considered adequate. A schematic illustrating the sample geometries is shown in Fig. 1. The regions probed by FEM and EELS are indicated by a dotted bounding box. In the following experimental sections, the exact volumes of the films that are sampled by each technique will be calculated explicitly.

B. Specimen preparation

The DLC films were prepared by PECVD at Argonne National Laboratory using a self-bias voltage of −500 V and a chamber pressure of ~10 mTorr. The deposition procedure has been outlined previously[11,20] and will not be enlarged upon further here except to note that the deposited films consisted of an approximately 1 μm thick DLC layer deposited onto a ≈100 nm thick Si bond layer previously deposited onto a clean (100) Si substrate. Plan-view samples were prepared by mechanical thinning from the back side with a dimple grinder to a thickness of ~10 μm and then ion milling in a Gatan precision ion polishing system (PIPS) using 3 kV Ar^+ ions. A thin piece of Mylar was employed to protect the front surface from redeposition of material during ion milling. The ion beams were directed at a glancing angle onto the back side of the sample to minimize beam damage and preserve the surface volume of the film. Prior to preparation as cross sections, a thin gold marking layer was evaporated onto the surface of the films. Two pieces of sample were then glued together face to face. The gold layer ensured that the DLC remained distinct from the glue in the TEM. These cross-sectional samples were mechanically thinned into a wedge using a Southbay polisher and then ion milled in the PIPS from both sides using 3 kV Ar^+ ions directed at a glancing angle. Times in the ion mill were short at approximately 20 min. Ion milling was chosen as the method for specimen preparation for these films as they are impervious to both acidic and basic solutions, withstanding up to 40 h in an HF bath.[25,26]

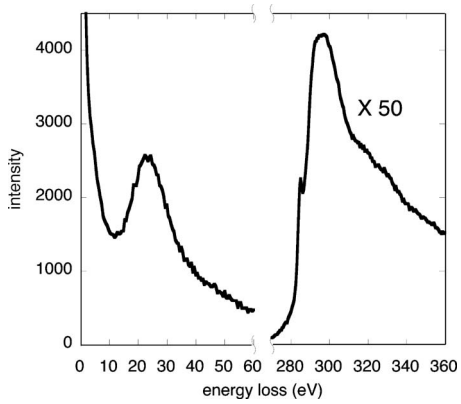

FIG. 2. A typical EEL spectrum from the DLC films studied in this investigation. The low-loss region displays the zero-loss peak and the first plasmon peak at ~22 eV. The core loss region of the spectrum (shown stripped) contains the peak due to the $1s \rightarrow \pi^*$ transition at 285 eV and the extended region due to the $1s \rightarrow \sigma^*$ transitions beginning at 290 eV. The mass density and $sp^2:sp^3$ carbon bonding ratio were extracted from such spectra as described in the text.

C. EELS

Parallel electron-energy-loss spectroscopy was performed in a Philips CM30T operating at 100 keV using a Gatan 666 parallel electron-energy-loss (PEEL) spectrometer. PEEL spectra were recorded in diffraction mode using convergence and collection semiangles of 3 and 5 mrad, respectively. A crushed and dispersed graphitized carbon sample was used as the 100% sp^2 reference sample. Both the low-loss and carbon K-edge spectra were recorded from each area using acquisition times of 0.05 and 15 s, respectively. A representative electron-energy-loss (EEL) spectrum is shown in Fig. 2. The features in this spectrum are typical of low-density hydrogenated DLCs.[27] In the low-loss spectrum, there is the plasmon peak at approximately 22–23 eV and in the core

loss region a peak at 285 eV due to transitions from the filled $1s$ level to the empty π orbitals and a broader feature due to transitions from the $1s$ level to the empty σ orbitals.

After removal of the zero-loss peak, the position of the plasmon peak was used to calculate the mass density of the films according to

$$E_p = \hbar\left(\frac{n_e e^2}{\epsilon_0 m^*}\right)^{1/2}, \tag{1}$$

derived assuming a "quasifree" electron model for the valence electrons.[28] E_p is the plasmon energy, $\hbar$ is the reduced Planck constant, n_e is the valence electron density, e is the electron charge, ϵ_0 is the dielectric function of free space, and m^* is the effective mass of the electron. The valence electron density is calculated assuming that carbon contributes four valence electrons and hydrogen one valence electron. The atomic fractions of carbon and hydrogen were estimated from the HFS data.[11] These parameters are not available for NFC10, and so a value of 40 at. % was used for the atomic fraction of hydrogen in this case. The value for the effective mass of the electron was estimated as $0.7m$, where m is the mass of a free electron. This value is appropriate for hydrogenated DLC films with such a high proportion of hydrogen.[27] The refractive index at zero frequency $n(0)$ may be used to obtain a better estimate for m^*.[27] Such measurements have not yet been undertaken for these films.

The carbon K-edge region of the spectrum was treated with a background removal and a deconvolution with the low-loss spectrum to remove multiple scattering. The ratios of $sp^2{:}sp^3$ carbon bonding in the samples were determined using the integrated counts in the $1s \rightarrow \pi^*$ peak, N_{π^*}, normalized to the total number of counts in the $1s \rightarrow \pi^*$ and $1s \rightarrow \sigma^*$ regions of the spectrum, $N_{\pi^*}+N_{\sigma^*}$, together with the same quantity from the 100% sp^2 sample.[27] The procedure is summarized by

$$\%\, sp^2 = \frac{\left(\frac{N_{\pi^*}}{N_{\pi^*}+N_{\sigma^*}}\right)_{sam}}{\left(\frac{N_{\pi^*}}{N_{\pi^*}+N_{\sigma^*}}\right)_{ref}} \times 100. \tag{2}$$

The integration windows used for the $1s \rightarrow \pi^*$ and the $1s \rightarrow \sigma^*$ regions of the spectra were 283–287 and 283–303 eV, respectively. Some authors employ the areas of two Gaussians to calculate the relative contributions of the $1s \rightarrow \pi^*$ transition and the $1s \rightarrow \sigma^*$ transition.[29,30] Since there appears to be no clear preference for this approach, we have chosen instead to use the integrated counts.

The energy-loss near-edge structure (ELNES) of the graphite carbon K-edge changes as a function of crystal orientation relative to the incident beam direction. These changes depend also on the convergence and collection semiangles. The selection of electrons that have undergone a certain momentum exchange by the angular constraints of the microscope conditions alters the cross section for the $1s \rightarrow \pi^*$ transition relative to the cross section for the $1s \rightarrow \sigma^*$ transition. Theoretical modeling of the situation has led to the identification of "magic angle" measurement conditions which minimize or remove the angular dependence of the ELNES of graphite.[31–35] However, there is significant difference of opinion in these works about what constitutes the magic angle conditions with both experiments and theories diverging by a factor of 2. Our angular conditions for the EELS measurement of the ratios of $sp^2{:}sp^3$ carbon bonding do not correspond to the magic angle conditions that are prescribed. Given the lack of agreement about the correct conditions, we elected to sample many randomly oriented particles of graphite and obtain an orientational average of the carbon K edge of graphite in this way rather than employing magic angle conditions.[36]

The thickness of the regions probed using EELS may be determined using an estimated value of the inelastic mean free path of the electrons of 110 nm.[28] The thickness relative to the inelastic mean free path of the electrons was extracted from the low-loss spectra and it was found that the regions probed were 30–50 nm thick. Regarding the plan-view samples, this meant that the measured region was the topmost 30–50 nm of the films plus any adsorbed layer. In the case of the cross-sectional samples, measurements were taken in many different positions relative to the interface with the Si substrate. No difference was seen between the values as a function of film depth, and so these measurements are reported as an average. As explained earlier, we preferred to determine spatially averaged properties, and so a probe size of about 40 nm was used.

D. FEM

FEM was used to measure the degree of medium-range order in the samples. Tilted dark-field images were acquired on an automated system installed on a JEOL JEM-4000EXII. The images were treated with a Wiener filter prior to the calculation of the normalized intensity variance.[10,11] The intensity variance (var) of the images as a function of the tilt vector k (nm^{-1}) supplies a statistical measure of the pair-pair atomic correlation functions or medium-range order in the samples.[37] The interpretation of the features and magnitude of the var(k) plots is not straightforward. Unlike the average scattered intensity seen in diffraction patterns, the var(k) plots may not be directly inverted to obtain the correlation functions and additionally are hard to normalize for volume. In fact, the magnitude of the variance varies with specimen thickness in a way that is highly dependent on k.[38] This fact is plain when one examines the FEM plots shown in Fig. 3, which were obtained from a cross-sectional DLC sample that possessed uniform regions of different thicknesses. The thicknesses were calculated using an estimate of the elastic mean free path of the electrons of 400 nm and by measuring the normalized bright-field image intensity I/I_0.[39] An exponential decay of bright-field image intensity with thickness was assumed as shown in the left ordinate of part (b) of Fig. 3. The error in the thickness determinations was calculated using the standard deviation of the intensities and was at the level of 5% of the value.

The specific features of the var(k) plots will be discussed in more detail later. At this point, it is important to note only that the magnitude of the variance changes by greater than

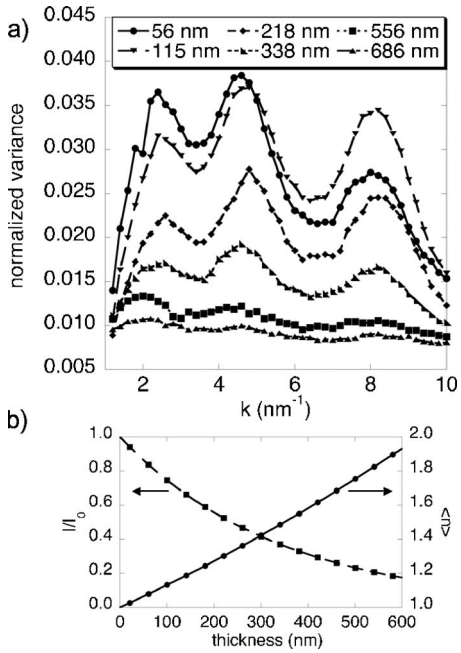

FIG. 3. (a) Variation of var(k) with specimen thickness. The magnitude of the variance changes with the thickness of the specimen in a way that is highly dependent on k. (b) Normalized bright-field image intensity I/I_0 and expectation number for the number of scattering events $\langle n \rangle$, as a function of thickness. At a thickness of 200 nm, the dark-field image of the DLC does not have a large component due to electrons that have undergone multiple scattering.

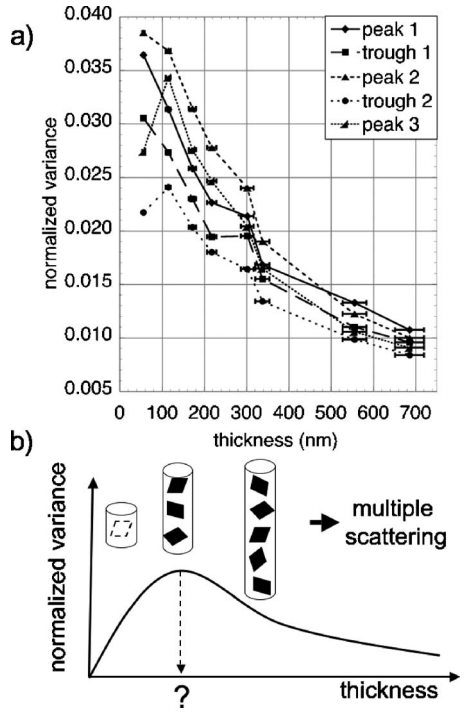

FIG. 4. (a) Variation of magnitude of certain features in the var(k) plot at certain values of k with thickness. Ratios of the sizes of two features will also change with thickness. (b) Depiction of the variation of the normalized variance with sample thickness. The curve shape arises by considering the origin of the contrast in the dark-field images.

threefold over the span of the thicknesses measured. Figure 4(a) plots the changes to the magnitude of the variance of certain features of interest in the variance plot as a function of thickness. These features are the three peaks at 2.7, 5, and 8.5 nm^{-1} and the troughs between these peaks at 3.3 and 6.2 nm^{-1}. It is clear by examining this plot that the magnitude of the variance changes with thickness in a way that is dependent on k. In particular, the peak magnitudes change more quickly than the trough magnitudes. This indicates that a ratio of feature heights will not be constant as the thickness changes.

The k-dependent variation of the intensity variance with thickness can be understood in the following way. The pixel-to-pixel intensity variation in a dark-field image depends upon the magnification or the area sampled by a pixel and the volume probed, which is defined by the thickness of the sample and the microscope resolution employed.[23] We shall assume that the resolution and magnification are kept constant and only the thickness is changed. At small thickness, the volume probed may or may not contain an ordered cluster oriented such that it reflects either strongly or weakly into that k, and so the normalized variance is comparatively low. As the thickness increases, the probability that a cluster is present in the volume likewise increases, and for a while, the intensity variance will also increase as it becomes more probable that a cluster will be within that volume to produce a scattered intensity at that k which differs extremely from the average. A maximum in the variance will be reached at a certain thickness. Subsequent to this point, there will be too many clusters present in the volume and they will act to average the scattered intensity at that k, reducing the variance. Note that this occurs well before multiple scattering begins to reduce the variance by altering the electron phases a number of times. The changes to variance with thickness according to this scheme are illustrated in Fig. 4. Using this scheme, we can also understand why the changes to the variance of the peaks occur more quickly with thickness than the changes to the variance of the troughs. It is because the regions of correlated structure scatter more strongly into these k. While the shape of this graph is universal, the actual curve is highly specific to the materials system. Cluster size, crystallinity, and density have impact on the slopes of the two sections of the curve and the position and height of the variance maximum.[38]

Comparing the shape of the plots in Fig. 4(a) with the hypothetical plot shape generated by our considerations of the process of contrast production in amorphous materials shown in part (b) of that figure, we see that only peak 2 and trough 3 seem to conform to the prediction of having a maximum in the variance with thickness. This situation is an artifact that has arisen due to the small scattering powers of the atomic constituents of these films and the subsequent low thickness contrast of these specimens. For the thinnest specimen area measured, the dark-field images at high incident beam tilt required extremely long exposure times and the specimen drift artificially reduced the image variance. Thus, it seems as though the low thicknesses at which the variance would initially grow and then peak are not accessible for this material. The shape of the variance vs thickness plot has

been confirmed previously both experimentally and theoretically for amorphous silicon.[38] For amorphous silicon, one data point in thickness below the variance maximum could be accessed allowing for a reasonable fitting of the graph. On the basis of this, a mapping procedure was suggested whereby all FEM data sets from samples of different thicknesses could be mapped to the same arbitrary thickness, thus reducing any errors arising from the thickness effect.[38] In our case, such a procedure is not feasible as we cannot access the full curve.

Due to these considerations, the FEM measurements performed in this work were done on areas that demonstrated the same thickness relative to the elastic electron mean free path. The thickness of the regions probed by FEM was determined to be 200 ± 30 nm.[39] While such a thickness is unusually large for any TEM study, the low contrast thickness of these materials meant that a thinner specimen would have required intolerably long dark-field exposure times. We can check if the conditions required to interpret the intensity variance of tilted dark-field images as measures of the pair-pair atomic correlation functions are still met.[37] These are that the electrons that comprise the image are singly scattered and that the object constitutes a weak phase object (WPO). The expectation number for the average number of scattering events $\langle n \rangle$ (Ref. 40) was calculated by assuming a Poisson distribution for the probability of a scattering event at a particular depth, and a value of 1.25 was obtained for this thickness. $\langle n \rangle$ as a function of thickness is displayed on the right ordinate of Fig. 3(b). This demonstrates that while electrons that have undergone multiple elastic-scattering events do contribute to the images, they do not form the dominant component. Their presence will act to reduce the intensity variance as noted above. The conditions for the WPO approximation can be relaxed for an amorphous material due to the fact that the electrostatic potential at a particular point does not diverge greatly from the average potential. This is unlike the case for crystalline materials in which the potential is peaked strongly above atomic columns. So, for amorphous materials, the zero of potential may be shifted to the average potential and the WPO approximation almost always applies for amorphous materials of low atomic number.[41]

At least ten different areas of the same nominal thickness per sample were examined using FEM. The standard error of the FEM values at each k was used as the error. So, for the plan-view samples, a surface volume of $240 \times 240 \times 200$ nm^3 is probed in the direction of the film normal. For the cross sections, volumes of the same magnitude were studied from a vantage point of parallel to the plane of the film, but either in the top or bottom halves of the films. The cross-sectional FEM results from the top and bottom halves of the films did not differ significantly for all the films, and so, similar to the EELS measurements, the overall average is displayed.

III. RESULTS

A. EELS: Short-range order

Figure 5 displays (a) the mass density and (b) the sp^2 carbon bonding fraction deduced using EELS for each of the DLC samples. Plan-view samples are denoted with a "pv" suffix, while cross-sectional samples are denoted with an "x" suffix. Note that the results are ordered; the amount of hydrogen in the source gas decreases from left to right. In these and the subsequent bar graphs displayed in this paper, the cross-sectional measurements are outlined with a heavy border to aid in the interpretation.

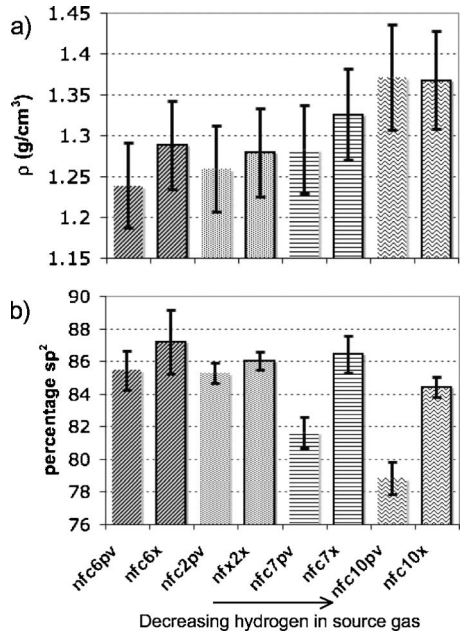

FIG. 5. (a) Mass density of the DLC films determined using the low-loss EELS spectrum. (b) Ratio of carbon sp^2:sp^3 bonding deduced from the carbon K-edge region of the EELS spectrum. The amount of hydrogen in the source gas decreases as one goes from left to right. Cross-sectional measurements are shown with a heavy black border. These conventions are retained in subsequent bar graphs. In general, a greater amount of hydrogen in the source gas encourages less dense DLC films with a higher absolute fraction of sp^2 bonding.

Considering first the mass density, some general remarks may be made. The measured densities are in accord with but tend to be slightly lower than those measured for other DLC films made under similar conditions[4,17] and with previous determinations of the mass density of these specific films by neutron reflectivity.[19] As noted above, the density of hydrogenated DLCs determined using the EELS technique is highly sensitive to the value of the effective mass m^*. Here, a value of 0.7 was used, which is the minimum appropriate for *polymeric* hydrogenated DLC with such a high proportion of hydrogen.[16] There is evidence to suggest that the NFC films, while they contain high proportions of hydrogen, diverge significantly in structure and properties from polymeric hydrogenated DLCs with comparable amounts of hydrogen.[18] m^* for the NFCs could take values in the upper region of the range 0.7–0.87, with 0.87 being the value for hydrogen-free amorphous carbon. Values of m^* closer to 0.87 would yield a range of densities for the NFCs some 15% higher, closer in value to other determinations.[17,19] As an additional check, we can use the linear relation between the

mass density and the full width at half maximum of the G peak [FWHM(G)] in the UV Raman spectrum, derived for hydrogenated amorphous carbons with $H>20$ at. %.[18] The FWHM(G) may be estimated[11] as 100–110 cm^{-1}, yielding a density of 1.36–1.47 g/cm^3, corroborating our findings.[18]

The EELS data indicate a trend in mass density with source gas composition. A higher absolute proportion of hydrogen in the source gas either by using a hydrocarbon that contains more hydrogen or by the addition of extra hydrogen gas lowers the mass density. This trend matches the neutron reflectivity measurements of the bulk of the films. The neutron reflectivity measurements also discovered a much denser (2–2.5 g/cm^3) 30 Å thick surface layer on all of the films. This surface layer increased in density as the hydrogen proportion in the source gas increased. The thickness probed by EELS is 30–50 nm, and so such a layer is not resolved clearly in the present plan-view measurements. The presence of a thin high-density surface layer might be expected to give a 1% increase in the measured plan-view mass density which is below the sensitivity of our measurement.

Part (b) of Fig. 5 displays the calculated percentage of carbon sp^2 bonding for each of the samples. All of the samples possess extremely high percentages of sp^2 carbon bonding. This is somewhat surprising for such low-density, high hydrogen content DLC films.[4,27] Generally, such high hydrogen content DLC films are classed polymeric and have both a high percentage of sp^3 carbon bonding, which is stabilized by the presence of hydrogen, and extremely low mass densities. The high percentage of sp^2 bonding may be further evidence that these films represent a unique class of highly hydrogenated, highly graphitic DLC films.[18] Indeed, if we use the correlation between the FWHM(G) and the dispersion in the Raman G peak, disp(G), and then the relation between disp(G) and the sp^3 bonding fraction, we obtain an estimate for the sp^3 fraction of 20%, which is very similar to that measured here.

There is not much to distinguish between the films in terms of the measured carbon bonding fractions presented here. Both the plan-view and cross-sectional specimens of NFC2 and NFC6 and the cross sections of NFC7 and NFC10 have carbon bonding fractions within the error of each other with values falling between 84% and 87%. The uncertainty estimates are the standard errors of approximately ten measurements from each sample. In general, there is a trend for the plan-view sample to display a lower sp^2 bonding fraction than the cross section. This is most striking in the case of NFC7 and NFC10. NFC7PV has an sp^2 carbon bonding fraction of 81%, while NFC10PV has an sp^2 bonding fraction of an even lower 79%. Near-edge x-ray absorption fine structure (NEXAFS) measurements using the electron yield were performed on NFC6 in an earlier experiment,[11] determining the percentage of sp^2 carbon bonding to be 69±2%. The apparent discrepancy with the results presented here can be attributed to the fact that electron-yield NEXAFS probes only the top 10 nm of the film[11] as opposed to the 30–50 nm we probe using EELS.

The EELS results can be summarized quite simply. There is a definite trend toward a lower bulk mass density with higher absolute proportions of hydrogen in the films. The films grown in the pure hydrocarbon atmospheres have a surface layer that possesses a much lower carbon sp^2 bonding fraction than the bulk of these films and also the surface and bulk of the films grown with additional hydrogen. NFC10, grown in acetylene, whose growth conditions correspond to the lowest absolute proportion of hydrogen in the source gas, has the surface layer with the lowest carbon sp^2 bonding fraction.

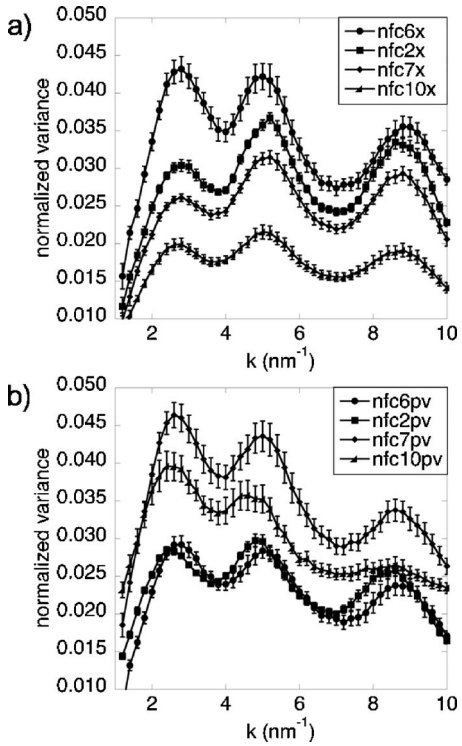

FIG. 6. FEM measurements of (a) cross-sectional samples and (b) plan-view samples of DLC. The magnitude of the variance indicates the relative degrees of medium-range order between the films. The peak at 2.7 nm^{-1} is associated with clusters that have graphitic short-range ordering, and the peaks at 5 and 8.5 nm^{-1} correspond to clusters with diamondlike structures. Parameters extracted from the var(k) plots are summarized in the next figure.

B. FEM: Medium-range order

Figure 6 displays the measured normalized intensity variance as a function of k for (a) the cross-sectional and (b) the plan-view DLC samples. Three broad peaks are evident in all the FEM plots, attesting to significant medium-range order in the specimens. If there is no ordering in the medium range, then the var(k) graphs generated by FEM are flat and featureless.[13] The first peak at ~2.7 nm^{-1} has been ascribed to clusters with graphitic local bonding (largely sp^2), while the features at 5 and 8.5 nm^{-1} have been associated with structural units containing local diamondlike ordering (largely sp^3).[10] These interpretations are valid for hydrogen-free DLCs and can be used to describe these samples, even though they contain a significant proportion of hydrogen, as we will now demonstrate.

It has been shown that an analytical expression for the intensity variance can be readily obtained from the dark-field

image wave function which consists of the sum of the wave functions from individual atomic scatterers.[9] For an amorphous material containing one constituent atom, this results in an expression for the variance that is weighted by the atomic scattering factor raised to the power of 4, f^4. This approach can be generalized for an amorphous material containing two constituent atoms, resulting in an expression for the variance containing mixed sums and weighted by the appropriate combinations of the atomic scattering factors f_A^4, f_B^4, $f_A^3 f_B$, $f_A f_B^3$, and $f_A^2 f_B^2$ for atoms A and B, respectively. In the case of the DLCs that are being studied in this work, the interpretation of the intensity variance may be simplified by using the fact that the atomic scattering factor for hydrogen is approximately five times smaller than the atomic scattering factor for carbon over the angular range that is probed.[42] Thus, the FEM will be 625 times more sensitive to the purely carbon correlations than to hydrogen atomic correlations and 5–125 times more sensitive to the purely carbon correlations than to mixed atomic correlations. This justifies our interpretation of the features in the FEM plots as due predominantly to clusters with graphitic or diamondlike local ordering.

As a general rule, the larger the peak magnitude in the var(k) plot, the higher the degree of medium-range order. More specifically, the heights and widths of the features vary depending upon the resolution employed for the experiment, the size distribution of the clusters, the number of clusters, and the "crystallinity" of the clusters. Additionally, these quantities do not act in isolation upon the appearance of the FEM data. For example, a certain resolution may interact positively with a certain cluster size to enhance the magnitude of the FEM signal at a particular k. When comparing samples made via a similar process and with similar properties, it is tempting to assume that the kind of medium-range order is the same, that is, that the cluster size distribution and crystallinity are constant. This practice can lead to error. This is especially the case with a carbon compound as the different hybridizations of carbon allow for abrupt changes in structure and ordering as some parameters of growth or processing are changed continuously. An example of this is the transition from stage 2 to stage 3 in the phenomenological three-stage model of Ferrari and Robertson.[16] This model describes the transformation of graphite to tetrahedral amorphous carbon (ta-C) or highly ta-C by further amorphization via ion implantation. Equally, it describes the opposite trajectory from ta-C to graphite via ordering processes such as annealing, but the two trajectories are not equivalent and some hysteresis exists. As the material passes from stage 2 to stage 3, it is transformed from amorphous carbon to ta-C. During this process, the size of the graphitic clusters diminishes from rings to chains and eventually sp^2 dimers. It appears that the onset of stage 3 is quite abrupt as the curves describing the position of the Raman G peak and the ratio of the intensity of the D peak to the intensity of the G peak, $I(D)/I(G)$, have discontinuities in their derivatives at this point. Thus, it would not be accurate to assume that the graphitic clusters possess the same medium-range order across this boundary.

Given these considerations in our interpretation of the FEM data, we will refer to graphitic medium-range order and diamondlike medium-range order as we discuss the differences between the DLC samples. For example, an increase in the degree of graphitic medium-range order will indicate that either the size, number density, or crystallinity of clusters with graphitic local bonding has increased and make explicit the fact that these possibilities cannot be distinguished from the experimental results alone. We will define some parameters for ease of comparison. The height of the peaks in the var(k) plots will be used as a measure of the degree of medium-range order. The degree of graphitic medium-range order (DMRO_g) is defined as the height of the peak at 2.7 nm^{-1}, while the degree of diamondlike medium-range order (DMRO_d) is defined as the amplitude of the peak at 5 nm^{-1}. The total degree of medium range order (DMRO) is the sum of these quantities. The relative proportions of graphitic to diamondlike medium-range orders is given by $\frac{\mathrm{DMRO}_g}{\mathrm{DMRO}_d}$. These parameters are extracted from Fig. 6 and presented in Fig. 7.

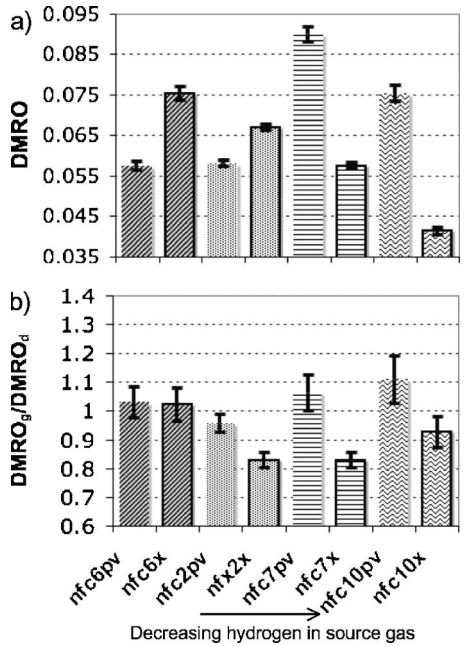

FIG. 7. Summary of parameters extracted from the FEM plots. (a) Overall degree of medium-range order DMRO. (b) Ratio of the degree of graphitic medium-range order to the degree of diamondlike medium-range order, $\frac{\mathrm{DMRO}_g}{\mathrm{DMRO}_d}$. NFC6 and NFC2 possess more long-range homogeneity than NFC7 and NFC10 as the difference between the DMRO and $\frac{\mathrm{DMRO}_g}{\mathrm{DMRO}_d}$ from the plan-view and cross-sectional samples is less.

Turning first to the cross-sectional samples, it is clear that there is a trend with source gas composition with bulk NFC6 possessing the largest overall degree of medium-range order, and NFC10 the least. Further, NFC2X, NFC7X, and NFC10X have smaller relative amounts of graphitic medium-range order as compared to the level of diamondlike medium-range order. In NFC6X, the opposite is obtained. From the plan-view measurements, we see that the surface regions of NFC2 and NFC6 possess much lower DMRO than both NFC7 and NFC10, in contrast to the measurements from the bulk where there is a monotonic decline in DMRO with decreasing proportion of hydrogen in the source gas.

However, all the films show approximately the same $\frac{\mathrm{DMRO}_g}{\mathrm{DMRO}_d}$ in the volumes probed by the plan-view FEM measurements. We can also examine patterns in film homogeneity from the parameters extracted from the var(k) plots. For example, NFC6 and NFC2 have surface layers with a lower DMRO than their bulk, in contrast to the results for NFC7 and NFC10. Also, NFC6 and NFC2 seem to possess greater long-range homogeneity as the differences between DMRO and $\frac{\mathrm{DMRO}_g}{\mathrm{DMRO}_d}$ in the plan-view and cross-sectional measurements are lesser.

We have discussed the changes to the FEM results largely in terms of changes to the size, crystallinity, and number density of clusters with particular local bonding configurations. It is possible that an orientation bias of the clusters may also play a role in the reversals and contrasts that we detect in the FEM data. For example, graphitic clusters in as-deposited highly tetrahedral DLC (ta-C) are oriented with their c axes parallel to the plane of the film if the deposition is conducted at elevated temperatures. After annealing and the removal of compressive stresses, the clusters realign their c axes to be perpendicular to the film plane.[4,7,8] Consistent with these previous observations, we will limit this discussion to possible orientational bias of the clusters with local graphitic bonding. The strong anisotropy inherent in the graphitic structure coupled to the in-plane stresses of the films means that anisotropy of the graphitic structural units is much more likely than anisotropy of the units with local diamondlike bonding. Examining the FEM results, the only situation that may be consistent with anisotropy is the change in the $\frac{\mathrm{DMRO}_g}{\mathrm{DMRO}_d}$ parameter from high to low as one goes from the plan-view measurement to the cross-sectional measurement in the cases of NFC2, NFC7, and NFC10. Closer examination of this theory demonstrates that anisotropy is probably not a factor in this trend. The peak at 2.7 nm^{-1} has been related to the 0002 reflection in graphite that corresponds to the interplanar spacing of the graphene sheets. If the higher level of graphitic medium-range order seen in the plan-view samples of NFC2, NFC7, and NFC10 is due to anisotropy, then the graphitic clusters would have to be arranged with their c axes preferentially aligned to the plane of the film. In plan view, the c axes of the clusters will in each case be perpendicular to the electron beam, but can be rotated by any amount in the plane normal to the electron beam. The FEM in this work comprises the collection of tilted dark-field images with the series of tilts corresponding to a unidimensional scan of k space. Thus, only a small proportion of the graphitic clusters will be oriented such that they will scatter into this direction and so contribute to the FEM measurement. In cross section, the c axes can take any direction with respect to the electron beam subject to the constraint that they lie in the plane of the film. Again, a tiny proportion will be aligned such that they will reflect into the direction defined by the unidimensional angular scan. The difference between the number of graphitic clusters favorably aligned in the plan-view and cross-sectional measurements is a fraction of 1% even assuming that there is perfect alignment of all the clusters. The effect of this difference on the magnitude of the peak in the var(k) plot at 2.7 nm^{-1} is probably not great enough to account for the observed 20% effect in the data. Thus, we attribute the FEM results here to changes in size, crystallinity, and number density of clusters as a function of the volumes probed. We note also that anisotropy is not detected in the selected area electron-diffraction patterns of the cross sections (not shown). The existence of anisotropy would result in arcs of greater intensity in the scattered intensity for particular k's. As-deposited hydrogenated DLCs generally possess low internal stress in comparison to hydrogen-free amorphous carbons.[43] Thus, the driving force for the preferential alignment of the graphitic clusters is largely absent for the set of deposition parameters used here. A clearer signature of anisotropy would be obtained in the converse case of graphitic clusters aligned with their c axes to the film normal. In this instance, depending on the degree of alignment and the direction of the angular scan, a difference of close to 100% in the proportion of favorably aligned clusters may be obtained between the cross-sectional and plan-view orientations.

IV. DISCUSSION

A. Energetics of film growth

The structure and properties of hydrogenated DLC films depend critically on the growth parameters of the absolute amount of hydrogen in the source gas and bias voltage.[4] We will consider our results in the light of these parameters.

The absolute proportion of hydrogen in the source gas dictates film properties in several ways.[4] Greater absolute proportions of hydrogen in the source gas results in larger amounts of hydrogen incorporated into the subsequent film in general. This will tend to lower the film density. The presence of hydrogen also acts to stabilize the sp^3 carbon network as the hydrogen saturates the sp^3 sites. The inclusion of hydrogen in the films is moderated by the bias voltage in two ways. Firstly, ions penetrate the film more deeply as the bias voltage is increased. These ions can abstract atomic hydrogen from C-H bonds.[44] The atomic hydrogens combine to form hydrogen gas molecules that escape the surface. Thus, as the bias voltage is increased, the final hydrogen content is decreased. From the HFS measurements of our films, we know that the hydrogen content is constant within 10% for the source gas compositions studied. Thus, the effects of net increases in hydrogen to lower density and allow more sp^3 bonding configurations may be secondary in these films.

A second and perhaps more important consideration is how the bias voltage tunes the energy of the impinging carbon ions. The effective energy of the carbon ions in the plasma is a key quantity in determining exactly how close to diamond the properties of a DLC film will approach. This fact is well accounted for by the subplantation model. Central to the subplantation model is the idea that a highly sp^3 bonded underlayer is formed from the shallow implantation or subplantation of C^+ ions from the plasma. As the film grows, the less dense surface layer is continually transformed by subplantation into a denser, sp^3-rich under layer, resulting in a material that possesses some of diamond's striking properties. The key parameter in the subplantation model is the effective energy of the carbon ion, and it has been found that more diamondlike properties such as hardness, sp^3 content,

high mass density, and large optical gap are promoted when the carbon ion energy approaches a value of ~100 eV.[4,45] On either side of this energy, the diamondlike properties diminish.

The energy per singly charged carbon ion E/C^+ may be estimated for our deposition parameters and methane and acetylene atmospheres.[4,45] In the pressure regime that we are operating in, the average ion energy may be approximated by 0.4 of the bias voltage.[46,47] At lower operating pressures, the average ion energy approaches the bias energy as there are fewer collisions in the plasma. We assume that the carbon atoms impinge on the surface as methyl radicals in the case of the methane atmospheres[44,48] and as $C_2H_x^+$ ions in the case of the acetylene atmosphere.[45] As they impact the surface, the molecular ions break into their constituents with the energy being shared proportional to mass. We neglect the presence of hydrogen to gain an estimate of the effective energy of the carbon ions as follows:

$$\left(\frac{E}{C^+}\right)_{\{CH_4\}} \sim 0.4 \times V_b = 200 \text{ V}, \tag{3}$$

$$\left(\frac{E}{C^+}\right)_{\{C_2H_2\}} \sim \frac{1}{2} \times 0.4 \times V_b = 100 \text{ V}. \tag{4}$$

Here, V_b is the self-bias voltage. The estimated E/C^+ for acetylene is closer to the optimal value for diamondlike properties of 100 eV. This explains the tendency of NFC10 toward a higher mass density. It is also consistent with NFC10 and especially NFC10PV having a lower sp^2 carbon bonding fraction. However, a more complete understanding of the properties of the films may be obtained by considering the dual action of the hydrogen ions and the carbon ions. For example, NFC7X and NFC10X have higher percentages of sp^2 carbon bonding than their respective plan-view samples. This may be related to modifications wrought by the more penetrative hydrogen ions to the dense subplanted layer formed by the carbon ions during film growth. These considerations will be examined in a more quantitative fashion in the following discussion of the FEM results.

While parameters such as the density and the short-range order (as indicated by the ratio of carbon bonding) of DLC films have been discussed widely in the literature in the context of the energetics of the deposition process,[4] the medium-range order has not. There is every indication that bombardment of the growing film by ions present in the plasma may have a large effect on the medium-range order of the films. Amorphous silicon (*a*-Si) produced by keV self-ion-implantation of the crystalline phase[49] shows a large degree of medium-range order that may be removed via thermal annealing and structural relaxation.[50] The medium-range order has been identified with a "paracrystalline" state that results from the large undercooling in the center of the thermal spike associated with a collision cascade. Medium-range order has also been associated with low-energy ion irradiation. *a*-Si bombarded by low-energy (20 eV) argon ions during deposition shows increasingly large degrees of medium-range order as the ion flux is increased.[51,52] The argon ions are not energetic enough to penetrate the surface, and so, in this case, the irradiation is thought to enhance the atomic mobility on the surface, allowing more larger or more structurally ordered "paracrystallites" to form. The "spikes" used to describe the picosecond dynamics of ion impacts have predicted the formation of metastable structures in growing carbon films. Ions with an energy of only 100 eV can cause temperature spikes of ~4000 °C and pressure spikes of 10^{10} Pa.[26,53] The nonequilibrium structures that form in the spike volume are rapidly quenched with typical spike durations of order 10^{-11} s.

The plasmas used to grow the DLC films studied here contain a mixture of carbon and hydrogen ions. The hydrogen ion energies can be as low as a few eV for H^+ liberated from impacting CH_3^+ and $C_2H_x^+$ ions. There will also be H^+ ions with average energies of $0.4V_b$=200 eV from the breaking of hydrogen, methane, and acetylene gas molecules in the plasma. We have performed a Monte Carlo simulation with SRIM (Ref. 54) to simulate the interaction of carbon and hydrogen ions with the film. These simulations show that for the 200 and 100 eV carbon ions, the ion ranges, electronic energy loss, and nuclear interactions are confined to the first ~3 or ~2 nm, respectively. The ~200 eV hydrogen ions penetrate much more deeply and interact with the first ~10 nm of the growing film. It is difficult to quantify the total effect of the ion interactions without having an accurate estimation of the ion flux; however, some general observations can be made from the SRIM simulations. The carbon ions undergo 10–20 times more collision events than the hydrogen ions and hence generate more of a collision cascade. The hydrogen ions, in contrast, lose 70% of their energy through ionization events. The fact that hydrogen ions interact electronically with the volume that has just hosted the collision cascades associated with the carbon ions may have many ramifications for the final structure of the growing film. This situation is depicted in Fig. 8. The figure shows film growth at one instant at t_1 and another later at $t_2 > t_1$. The surface volume that is modified by the shallow carbon implantation at t_1 is further modified by the ionization events due to the more penetrating hydrogen ions at t_2.

Figure 9 summarizes the trends in film structure identified through the EELS and FEM measurements. The films may be divided into two rough classes, those grown with a hydrogen and hydrocarbon source gas admixture and those grown in a pure hydrocarbon atmosphere. In the diagram, the films are viewed in cross section. The dotted line in the films indicates the boundary between the plan-view and cross-sectional measurements, although we note that the observed differences could be due to the presence of an extremely thin surface layer or layers. In the diagram, background shading deepens with increasing absolute sp^3 carbon bonding, while clusters with local diamondlike and graphitic bondings are shown by tetrahedra and aromatic rings respectively. Larger DMRO is indicated by an increase in the size of these, and differing $\frac{\text{DMRO}_g}{\text{DMRO}_d}$ is shown by the respective numbers of clusters, although this is a graphical convenience. As discussed earlier, increasing DMRO and changes in $\frac{\text{DMRO}_g}{\text{DMRO}_d}$ can correspond to a number of things. Films grown with added hydrogen gas possess greater long-range homogeneity with differences between the percentage of sp^2 bonding, DMRO, and

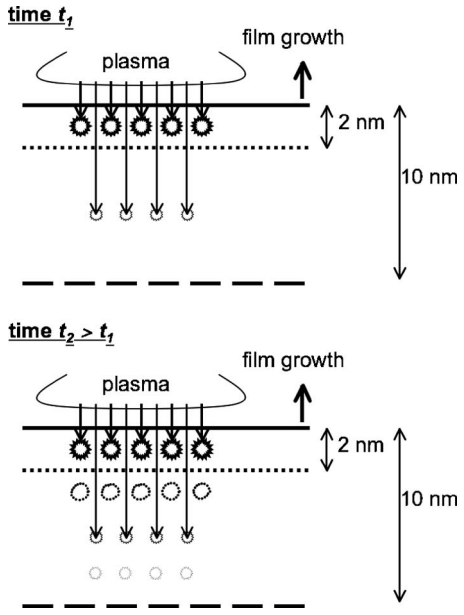

FIG. 8. Schematic illustrating the interactions of the ions from the plasma with the growing DLC film. The volume affected by carbon ion cascades at time t_1 undergoes further modifications at time $t_2 > t_1$ due to the predominantly electronic energy loss of the more deeply penetrating hydrogen ions.

$\frac{\mathrm{DMRO}_g}{\mathrm{DMRO}_d}$ being much slighter. In contrast to this, films grown in a pure hydrocarbon source gas have a surface layer with a greater DMRO and percentage of sp^3 bonding and a bulk with less DMRO and $\frac{\mathrm{DMRO}_g}{\mathrm{DMRO}_d}$. The fact that the percentage of sp^3 bonding is larger in the surface than in the bulk of these films while $\frac{\mathrm{DMRO}_g}{\mathrm{DMRO}_d}$ also increases highlights the intrinsic differences between these measurements. EELS is sensitive to bonding ratios, while FEM is sensitive to regions that have local graphitic and diamondlike bondings that are also structurally correlated.

We can explain some of these trends by considering the ion energetics on the structure of the resulting film. The relatively large collision cascades and thermal spikes produced by the carbon ions and the transient increase in density at the carbon ion range may produce preferable conditions for sp^3 bonding configurations and also relatively ordered clusters. As the film grows, the more penetrating hydrogen ions lose energy to ionization events as they traverse the layer modified by the carbon cascades; this may act to destroy some of the sp^3 bonding and DMRO. NFC6 and NFC2, grown with added hydrogen gas in the source gas, may be exposed to a greater flux of hydrogen ions, giving rise to greater long-range homogeneity and reduced DMRO in the surface. The increase in DMRO in the bulk of these films is an intriguing feature, given that hydrogen ions are thought to have a homogenizing effect. This may be related to the high flux of hydrogen ions that results in the overlapping of the small collision cascades associated with their end of range.

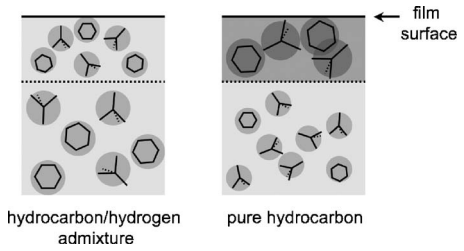

FIG. 9. The two broad classes of NFC films that are defined by the structural study presented in this paper. The plan-view measurement volume is indicated by a dotted line in the cross-sectional schematics. Deepening shading represents increasing sp^3 bonding fractions. Clusters with diamondlike local bonding are shown with tetrahedra, while clusters with graphitic local boding are indicated by aromatic rings. Increasing cluster size represents increasing DMRO, while $\frac{\mathrm{DMRO}_g}{\mathrm{DMRO}_d}$ is represented by the numbers of clusters.

Another factor which has yet to be considered is the chemical action of hydrogen at all depths it attains and the effect that this has on medium-range order. Hydrogen is extremely effective at abstracting bonded hydrogen.[44] Hydrogen ions with a large proportion of the bias energy modify structure to 10 nm. Atomic hydrogen and low-energy hydrogen ions liberated during the impact of hydrocarbon radicals interact with the surface and the first few nanometers of the film.[4] These two depth regimes for hydrogen penetration give rise to distinct zones in the growing film: a chemical zone at the surface and an ion zone at the depth that the hydrogen ions may penetrate to.[55] The abstraction of hydrogen from deeper in the film by the higher-energy hydrogen ions creates dangling bonds allowing for structural modifications to occur. Such modifications may increase the medium-range order in the bulk of NFC6 and NFC2 relative to the surfaces of these films. Hydrogen could also increase the overall degrees of freedom of the structure through the hydrogenation of sp^2 bonded carbon. Saturated sp^2 bonds lack rotational freedom which has a constraining influence on the structure. The hydrogenation of a few of these bonds would increase the degrees of freedom of the structure and could have a significant effect on the medium-range order in the material. Greater spatial resolution in the FEM measurements may allow for the complex and synergistic effects of ion and chemical interactions with the growing DLC films to be investigated further. However, as noted earlier, FEM is a statistical measurement, and so attaining the spatial resolution required to do this may be prohibited by the very nature of the technique. Using STEM and nanodiffraction as means of statistically sampling the structure of the DLC film in cross section may allow the changes to medium-range order to be obtained with higher resolution.

B. Mechanical and tribological properties

The TEM studies presented here provide considerable insight into how the structure of these films relates to their observed mechanical properties. Table I summarized film properties, showing that increasing hydrogen in the source gas provides a film that is less hard and has a lower coefficient of friction. The EELS measurements demonstrate that the harder films are denser and possess a surface layer with a higher proportion of sp^3 carbon bonding. A high coefficient of friction is also correlated with these highly sp^3 bonded

surface layers. The presence of σ bonds at the surface may play a role in the increased coefficient of friction for these films. Covalent bonding to dangling σ bonds represents the strongest interaction in carbon-based materials and accordingly can increase the coefficient of friction a great deal.[43] It has been thought that hydrogenation can compensate for this somewhat, as the hydrogen saturates dangling σ bonds.[43] In this case, bulk hydrogenation seems not to be the key as all the films measured by HFS possess the same hydrogen content. Moreover, it seems unlikely that the heightened proportion of sp^3 carbon bonding in the surface layer is the only reason for a high coefficient of friction as the increase in the percentage of sp^3 carbon bonding is only 4%–6%.

FEM measurements demonstrate that there are significant differences in the medium-range orders of the films. The softer, less dense films are more homogeneous in the long range, possessing less distinctions between the surface layer and the bulk. The surface layers of these films also have a lesser DMRO. In contrast, the films grown in pure hydrocarbon atmospheres have surface layers with much larger degrees of medium-range order than their bulk. Such ordering in the medium range might contribute to their high coefficients of friction. The inherent smoothness of DLC films is known to reduce frictional forces.[43,56] Such smoothness is achievable due to the amorphous nature of the material. However, as we see here, there can be large differences in the structure of amorphous materials in the medium range. Such inhomogeneity in the medium range may contribute a great deal to the coefficient of friction, which is, after all, a parameter that summarizes interactions at many scales, from those between individual atoms to those between the much larger surface features that constitute roughness. In this case, granularity at the 1–3 nm length scale might play a role in determining the friction properties of the films.

C. Raman spectroscopy

We can begin exploring the relationship between the features seen in the Raman spectrum of these DLC films and the FEM results presented here. UV Raman spectroscopy was performed on the films grown in the methane and methane and hydrogen gas admixtures.[11] As the fraction of hydrogen in the source gas increases, very few changes are apparent in the UV Raman spectrum. Both the *G* peak position (1595 cm^{-1}) and the intensity of the *D* peak relative to the intensity of the *G* peak stay the same. The high *G* peak position and the presence of the *D* peak indicate that sp^2 bonded carbon is present in disordered rings. The fact that the Raman results indicate little variation between the films in contrast to the FEM results is perhaps not surprising for two reasons. Firstly, Raman spectroscopy probes the whole thickness of the film and averages the signal over any distinct layers that may exist. Secondly, Raman spectroscopy and FEM will have different sensitivities, even though they are both sensitive to clustering, and as discussed earlier, comparison of the two is not straightforward. A recent article categorizes hydrogenated DLCs according to their structure and properties and correlates these to their multiwavelength Raman spectra.[18] In that work, the NFCs are found to be unique in that they possess both a high hydrogen content and a ringlike sp^2 configuration. This unusual combination is found optimal for friction properties. Correspondences between that work and the FEM results presented here will be explored in a future work. Indeed, the current work highlights the need for a systematic study comparing the results from Raman spectroscopy and FEM on DLC films.

V. CONCLUSIONS

The FEM and EELS measurements on these films demonstrate that many subtle growth processes contribute to the eventual structure and properties of a hydrogenated DLC film. It appears that homogeneity at all scales is found in films with low coefficients of friction. The films with the highest friction coefficients possessed a very distinct layered structure with discernable differences between both the local bonding and the medium-range order of the surface volume compared to the bulk of the film. The surface layers of these films had slightly elevated levels of sp^3 carbon bonding and were also more structured in the medium range. Greater homogeneity in the films with low coefficients of friction was related to the action of the increased flux of hydrogen ions in the plasma. The passage of hydrogen ions through the surface layer damaged by the less penetrative carbon ions during film growth relaxes the regions of more highly correlated structure. A more precise knowledge of the populations of ions in the plasma and their fluxes and energies might illuminate this effect further. A general challenge in the characterization of medium-range ordering in DLC films is to explore the correspondence between the sensitivities of Raman spectroscopy and FEM.

ACKNOWLEDGMENTS

We would like to acknowledge the insights of J. M. Gibson during a fruitful discussion. This work was supported in part by the U.S. Department of Energy under Contract No. DE-AC02-06CH11357 at ANL. The transmission electron microscopy was conducted in the Electron Microscopy Center at Argonne National Laboratory.

*Electronic address: aliu@anl.gov

[1] M. A. Tamor, W. C. Vassell, and K. R. Carduner, Appl. Phys. Lett. **58**, 592 (1991).
[2] T. Schwarz-Selinger, A. von Keudell, and W. Jacob, J. Appl. Phys. **86**, 3988 (1999).
[3] M. P. Seigal, J. C. Barbour, P. N. Provencio, D. R. Tallant, and T. A. Freidmann, Appl. Phys. Lett. **73**, 759 (1998).
[4] J. Robertson, Mater. Sci. Eng., R. **37**, 129 (2002).
[5] A. Libassi, A. C. Ferrari, V. Stolojan, B. K. Tanner, J. Robertson, and L. M. Brown, Diamond Relat. Mater. **9**, 771 (2000).

[6] C. A. Davis, G. A. J. Amaratunga, and K. M. Knowles, Phys. Rev. Lett. **80**, 3280 (1998).
[7] A. Illie, A. C. Ferrari, T. Yagi, S. E. Rodil, J. Robertson, E. Barborini, and P. Milani, J. Appl. Phys. **90**, 2024 (2001).
[8] Y. Lifshitz, G. D. Lempert, E. Grossman, I. Avigal, C. Uzan-Saguy, R. Kalish, J. Kulik, D. Marton, and J. W. Rabelais, Diamond Relat. Mater. **4**, 318 (1995).
[9] M. M. J. Treacy, J. M. Gibson, L. Fan, D. J. Paterson, and I. McNulty, Rep. Prog. Phys. **68**, 2899 (2005).
[10] X. Chen, J. P. Sullivan, T. A. Freidmann, and J. M. Gibson, Appl. Phys. Lett. **84**, 2823 (2004).
[11] J. A. Johnson, J. B. Woodford, X. Chen, J. Andersson, A. Erdemir, and G. R. Fenske, J. Appl. Phys. **95**, 7765 (2004).
[12] M. M. J. Treacy, J. M. Gibson, and P. J. Keblinski, J. Non-Cryst. Solids **231**, 99 (1998).
[13] P. M. Voyles, N. Zotov, S. M. Nakhmanson, D. A. Drabold, J. M. Gibson, M. M. J. Treacy, and P. Keblinski, J. Appl. Phys. **90**, 4437 (2001).
[14] J. M. Cowley, Ultramicroscopy **90**, 197 (2002).
[15] G. Y. Fan and J. M. Cowley, Ultramicroscopy **21**, 125 (1987).
[16] A. C. Ferrari and J. Robertson, Phys. Rev. B **61**, 14095 (2000).
[17] M. A. Tamor and W. C. Vassell, J. Appl. Phys. **76**, 3823 (1994).
[18] C. Casiraghi, A. C. Ferrari, and J. Robertson, Phys. Rev. B **72**, 085401 (2005).
[19] J. A. Johnson, J. B. Woodford, A. Erdemir, and G. R. Fenske, Appl. Phys. Lett. **83**, 452 (2003).
[20] A. Erdemir, O. L. Eryilmaz, and G. Fenske, J. Vac. Sci. Technol. A **18**, 1987 (2000).
[21] A. Erdemir, O. L. Eryilmaz, I. B. Nilufer, and G. Fenske, Surf. Coat. Technol. **133-134**, 448 (2000).
[22] W. E. McBride, D. R. McKenzie, D. G. McCulloch, D. J. H. Cockayne, and T. C. Petersen, J. Non-Cryst. Solids **52**, 257 (2005).
[23] W. E. McBride, Ph.D. thesis, University of Sydney, 2000.
[24] J. M. Cowley, Ultramicroscopy **90**, 197 (2002).
[25] A. Grill, B. S. Meyerson, and V. V. Patel, IBM J. Res. Dev. **34**, 849 (1990).
[26] H. Tsai and D. B. Bogy, J. Vac. Sci. Technol. A **5**, 3287 (1987).
[27] A. C. Ferrari, A. Libassi, B. K. Tanner, V. Stolojan, J. Yuan, L. M. Brown, S. E. Rodil, B. Kleinsorge, and J. Robertson, Phys. Rev. B **62**, 11089 (2000).
[28] R. F. Egerton, *Electron Energy Loss Spectroscopy in the Electron Microscope* (Plenum, New York, 1996).
[29] C. Souche, B. Jouffrey, G. Hug, and M. Nelhiebel, Micron **29**, 419 (1998).
[30] S. R. P. Silva, J. Robertson, Rusli, G. A. J. Araratunga, and J. Schwan, Philos. Mag. B **74**, 369 (1996).
[31] P. Schattschneider, C. Hébert, H. Franco, and B. Jouffrey, Phys. Rev. B **72**, 045142 (2005).
[32] N. K. Menon and J. Yuan, Ultramicroscopy **74**, 83 (1998).
[33] B. Jouffrey, P. Schattschneider, and C. Hébert, Ultramicroscopy **102**, 61 (2004).
[34] H. Daniels, A. Brown, A. Scott, T. Nichells, B. Rand, and R. Brydson, Ultramicroscopy **96**, 523 (2003).
[35] C. Hébert, B. Jouffrey, and P. Schattschneider, Ultramicroscopy **101**, 271 (2004).
[36] S. D. Berger, D. R. McKenzie, and P. J. Martin, Philos. Mag. Lett. **57**, 285 (1988).
[37] M. M. J. Treacy and J. M. Gibson, Acta Crystallogr., Sect. A: Found. Crystallogr. **52**, 212 (1996).
[38] P. M. Voyles, M. M. J. Treacy, J. M. Gibson, H.-C. Jin, and J. R. Abelson, in *Advances in Materials Problem Solving with the Electron Microscope*, edited by J. Bentley, U. Dahmen, C. Allen, and I. Petrov, MRS Symposia Proceedings No. 589 (Materials Research Society, Pittsburgh, 2001), p. 155.
[39] L. Reimer, *Transmission Electron Microscopy: Physics of Image Formation and Micoranalysis* (Springer-Verlag, Berlin, 1989).
[40] M. M. J. Treacy and J. M. Gibson, Ultramicroscopy **52**, 31 (1993).
[41] P. Buseck, J. Cowley, and L. Eyring, *High Resolution Transmission Electron Microscopy and Associated Techniques* (Oxford University Press, New York, 1988).
[42] L.-M. Peng, G. Ren, S. L. Dudarev, and M. J. Whelan, Acta Crystallogr., Sect. A: Found. Crystallogr. **52**, 257 (1996).
[43] A. Erdemir and C. Donnet, J. Phys. D **39**, R311 (2006).
[44] A. von Keudell, T. Schwarz-Selinger, and W. Jacob, J. Appl. Phys. **89**, 2979 (2001).
[45] M. Weiler, S. Sattel, K. Jung, H. Ehrhardt, V. S. Veerasamy, and J. Robertson, Appl. Phys. Lett. **64**, 2979 (1994).
[46] C. Wild and P. Koidl, J. Appl. Phys. **69**, 2909 (1991).
[47] C. Wild and P. Koidl, Appl. Phys. Lett. **54**, 505 (1989).
[48] T. Schwarz-Selinger, V. Dose, W. Jacob, and A. von Keudell, J. Vac. Sci. Technol. A **19**, 101 (2001).
[49] J.-Y. Cheng, J. M. Gibson, and D. C. Jacobson, J. Mater. Res. **16**, 3030 (2001).
[50] J.-Y. Cheng, J. M. Gibson, P. M. Baldo, and B. J. Kestel, J. Vac. Sci. Technol. A **20**, 1855 (2002).
[51] J. E. Gerbi, P. M. Voyles, M. M. J. Treacy, J. M. Gibson, and J. R. Abelson, Appl. Phys. Lett. **82**, 3665 (2003).
[52] P. M. Voyles and J. R. Abelson, Sol. Energy Mater. Sol. Cells **78**, 85 (2003).
[53] Y. Namba and T. Nori, J. Vac. Sci. Technol. A **3**, 319 (1985).
[54] J. F. Ziegler, http://www.srim.org, 2000.
[55] A. von Keudell, M. Meier, and C. Hopf, Diamond Relat. Mater. **11**, 696 (2002).
[56] M. Moseler, P. Gumbsch, C. Casirghi, A. C. Ferrari, and J. Robertson, Science **309**, 1545 (2005).